Supporting information

Individually Addressable Multichannel Nanoelectrodes Reveal Spatially Resolved Functional Heterogeneity of Vesicles in Single Cells

Chuchu Xu†[a], Ruolin Liu†[a,c], Yuhao Zheng[a], Yue Chen[a], Irina Svir[b], Alexander Oleinick[b,*], Zhongqun Tian[a,c], Christian Amatore[a,b] and Keke Hu[a,c,*]

[a]State Key Laboratory of Physical Chemistry of Solid Surfaces, College of Chemistry and Chemical Engineering, Xiamen University, Xiamen 361005, China

[b]Chimie Physique et Chimie du Vivant, Département de Chimie, École Normale Supérieure PSL University, Sorbonne Université, CNRS, 24 rue Lhomond, 75005 Paris, France

[c]Discipline of Intelligent Instrument and Equipment, Xiamen University, Xiamen 361005, China

†Equal contribution

Table of contents

Experimental

1. Chemicals and solutions

All reagents were purchased from Sigma-Aldrich unless otherwise specified. Isotonic solution: 150 mM NaCl, 5 mM KCl, 1.2 mM MgCl2 (Solaribo), 2 mM CaCl2, 5 mM glucose (Millipore) and 10 mM HEPES, pH 7.4, ~310 mOsm.

All components used for cell culture medium preparation were purchased from Gibco (USA). DMEM:Ham's F12 1:1 supplemented with 10% (v/v) fetal bovine serum, 1% (v/v) penicillin, 1% (v/v) cytosine β-Darabinofuranoside and 0.1% (v/v) 5-fuoro-2′-deoxyuridine.

2. Chromaffin cell and vesicle isolation

Bovine adrenal glands were obtained from a local slaughterhouse, and the chromaffin cells were isolated as previously described.[1] Briefly, the vein was perfused with Locke's buffer to clear away blood cells. The medulla was isolated after collagenase (0.2%, Sigma) treatment, and cells were isolated using a series of homogenization and centrifugation steps. For single cell experiments, ~500000 cells were seeded on 60 mm Poly-L-lysine (PLL) coated nunc dishes and maintained in a humidified incubator at 37 °C, 5% CO2 for a maximum of 3 days prior to experiments. Cells were rinsed with warm isotonic solution and maintained at 37 °C for amperometric experiments.

For vesicle isolation, a protocol developed by the Borges group was used.[2] Briefly, the medulla was mechanically homogenized in homogenizing buffer, and the vesicles were purified using a series of centrifugation steps: 1000g for 10 min to remove whole cells followed by 10000g to pellet vesicles. All centrifugation was performed at 4 °C. The final pellet of vesicles was resuspended and diluted in homogenizing buffer (100 μL vesicle suspension in 7 mL buffer) and subsequently used for electrochemical measurements the same day.

3. Fabrication of Four- and Thirteen-Channel Nanoelectrodes using CVD

(1) Hollow type:

Quartz capillaries were thoroughly cleaned and dried in the oven. The pulling parameters of P-2000 laser puller (Sutter, USA) were set as follows:

Line 1: HEAT = 820, FILAMENT = 4, VELOCITY = 14, DELAY = 128, PULL = 95,

Line 2: HEAT = 850, FILAMENT = 3, VELOCITY = 15, DELAY = 128, PULL = 45.

The resulting overall tip size of the pulled electrodes was approximately 500 nm. The pulling parameters were further adjusted as needed for different experiments. The pulled quartz capillaries were then placed in a tube furnace and heated to 960 °C for 20 min with a gas flow ratio of 300:180 (methane to argon, both gases were purchased from Linde), yielding hollow-type nanoelectrodes.

The 13-channel nanoelectrode array is fabricated from a seven-barrel quartz capillary (Sutter Instrument, 7Q033-16-10). During laser pulling, the seven primary lumens are preserved while confined interstitial domains are formed at the contact regions between adjacent barrels. After methane chemical vapor deposition (CVD), carbon is deposited along these confined regions, rendering them electrically conductive. As a result, in addition to the seven original lumens, six additional conductive nanochannels are generated at the interstitial positions, leading to a total of 13 individually addressable nanochannels at the tapered tip (see Fig. S2).

(2) Fully filled type:

The quartz capillary was positioned in the groove of the P-2000, and the parameters were set as follows:

Line 1: HEAT = 840, FILAMENT = 4, VELOCITY = 13, DELAY = 128, PULL = 95;

Line 2: HEAT = 900, FILAMENT = 3, VELOCITY = 15, DELAY = 128, PULL = 90.

The overall tip size of the pulled electrodes was within 100 nm. The pulling parameters were further adjusted as needed for different experiments. The quartz capillaries were then heated in a tube furnace at 980 °C for 50 min with a gas flow ratio of 200:200. Afterward, the electrodes were polished using a precision microelectrode polisher (MT-POLISHER100) to obtain smooth carbon surface.

(3) Polishing of fully filled four-channel nanoelectrodes

The electrode to be polished was vertically fixed on the holder. In manual mode, the descent distance was gradually adjusted so that the electrode approached the polishing surface while the turntable was operated at a rotation speed of 250 rpm. When the distance between the electrode tip and the polishing surface reached approximately 1–2 μm, the system was switched to automatic mode. The descent distance and speed were then programmed, and both parameters were fine-tuned during polishing according to the observed electrode surface condition.

4. Sample preparation and SEM imaging of nanoelectrodes

Nanoelectrodes were mounted vertically on the edge of the SEM stub using conductive adhesive tape, minimizing gaps between adjacent electrodes. An additional layer of conductive tape was applied to improve fixation and electrical contact. Scanning electron microscopy (SEM) imaging was performed on a field-emission microscope (GeminiSEM 500, Zeiss) under two orientations: vertically with the apex facing upward and at a 45° tilt. Images were acquired in both Inlens and SE2 modes with accelerating voltages of 3–5 kV (EHT) and aperture sizes of 20 or 30 μm. The working distance was maintained at 3–5 cm for Inlens mode and 5–7 cm for SE2 mode to ensure optimal resolution and surface morphology visualization.

5. Cell Staining

(1) Nuclear staining with Hoechst 33342

Cells were stained with Hoechst 33342 (PERFEMIKER) by mixing 2.4 mL of culture medium with 3 μL of Hoechst 33342 stock solution, followed by vortexing to ensure homogeneity. After cell adhesion, the medium was removed, and the cells were rinsed twice with PBS before incubation with the staining solution at 37 °C for 20 min. The dye was then replaced with an isotonic ionic buffer, and blue fluorescence of the nuclei was observed under a microscope using a 380 nm excitation light source and the corresponding filter set.

(2) Trypan blue staining

Cell viability before and after electrode insertion was assessed using trypan blue staining. A 0.4% trypan blue solution was directly added to the culture dish containing adherent cells at a 1:1 volume ratio with the existing buffer. After incubation at room temperature for 2–3 min, the cells were examined under an optical microscope. Viable cells excluded the dye and appeared transparent, whereas nonviable cells were stained blue due to membrane damage allowing trypan blue penetration.

6. Single cell insertion with four-channel open CNPs

Each channel of the four-channel nanoelectrode was inserted with a silver wire and positioned parallel on the electrode holder that was mounted on a micromanipulator with submicrometer resolution. The upper and lower two silver wires were connected to the headstages (In0 and In2) of the patch-clamp amplifier to ensure upper and lower regional distinction during cell insertion. The electrode was advanced toward the chromaffin cell under optical guidance using an inverted microscope (OLYMPUS IX73). During insertion, the nucleus was pre-labeled with a fluorescent dye to visualize its position and precisely control the insertion depth of the electrode relative to the nucleus. Under fluorescence excitation at 380 nm, the cell nuclei exhibited bright blue fluorescence under the microscope. After switching to bright-field mode, the electrode was inserted into the region just above the nucleus.

When the electrode tip first contacted the cell surface, nuclear fluorescence remained stable. Then a transient drop in baseline current appeared in the i–t trace, reflecting increased cellular resistance upon membrane penetration. After confirming entry, the electrode was further lowered by a few micrometers (typically 2–3 μm), then a slight scattering of the nuclear fluorescence could be observed if the tip penetrated too deeply, indicating contact with the nuclear envelope. To avoid this, the electrode was positioned just above the depth where nuclear scattering began, ensuring placement between the plasma membrane and the nucleus. However, when the tip was advanced excessively into the nucleus, amperometric spikes disappeared—consistent with the negligible catecholamine content within the nucleus—and nuclear fluorescence nearly vanished due to localized photobleaching and mechanical disturbance. Repeated trials determined the optimal insertion depth to be slightly above the nuclear membrane—typically 2–3 μm below the cell surface—ensuring minimal perturbation and reliable dual-site recordings within the cytoplasmic region.

7. Electrochemistry

(1) Cyclic voltammetry of four-channel open CNPs

Solution: 1 mM FcMeOH in 0.1 M KCl

Each channel of the four-channel nanoelectrode was inserted with a silver wire from the back and immersed in the electrolyte solution. Each channel formed an independent circuit with an Ag/AgCl counter/reference electrode. After all connections were completed, care was taken to ensure that the silver wires and electrode clips were electrically isolated from one another. Four potentiostats (Reference 620, Gamry) operated simultaneously to perform cyclic voltammetry.

After the simultaneous scans, the four silver wires connected to the respective channels were twisted together and linked to a single potentiostat as the working electrode to record the CV under the parallel configuration.

(2) Amperometric tests

In all amperometric experiments, a potential of +700 mV vs Ag/AgCl was applied using an Axon 700B potentiostat (Molecular Devices, San Jose, CA). All amperometric tests were conducted at 37 °C, controlled by a temperature controller (LINKAM Instruments). VIEC measurement of vesicular content in samples of isolated vesicles was done as previously described.[3] The CNPs were placed in a vesicle suspension solution and current transients were recorded.

8. Data acquisition and analysis

Current transients were recorded and digitized using a Digidata1550B (Molecular Devices) and digitized at 10 kHz or 100 kHz and filtered at 2 kHz using a 4-pole Bessel filter. The data were processed in IgorPro (Wavemetrics, Lake Oswego, OR).[3] Traces were manually checked for potential false detections done by the software. Spike characteristics were analyzed to quantify vesicular release events. The number of molecules released per spike was calculated from the integrated charge of each current transient using Faraday's law (N=Q/nF), where Q is the charge, n is the number of electrons transferred per molecule (here $n = 2$), and F is the Faraday constant. The half-width ($t_{1/2}$) was defined as the full width of the spike at half of its maximum amplitude, correlating with the release duration.

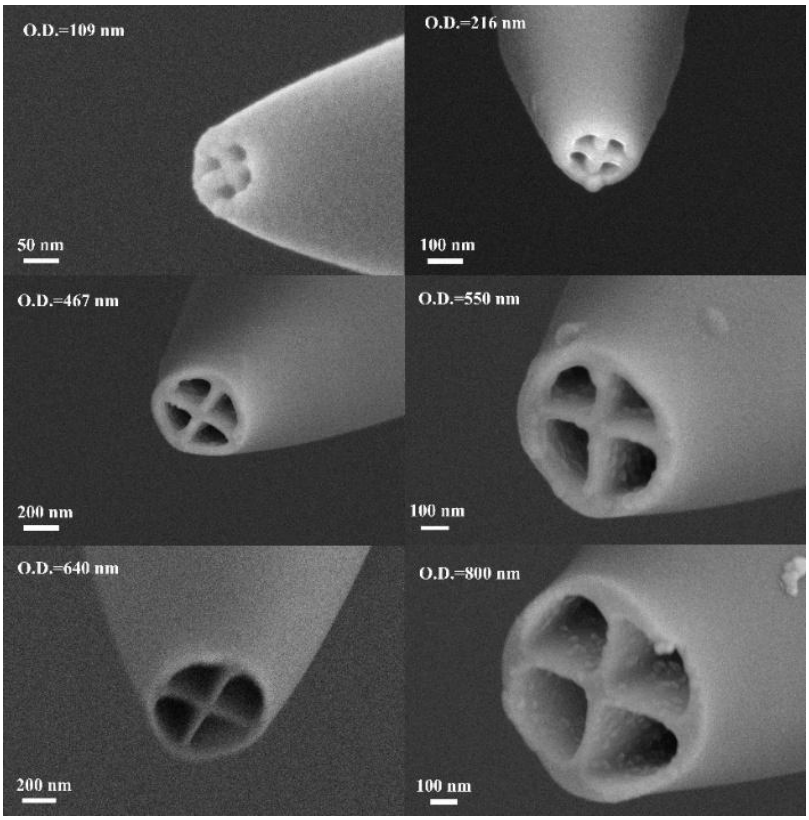

Figure S1. Representative SEM images of 4-channel open CNPs fabricated by catalyst-free CVD, showing precise control over outer diameter and channel geometry. The overall outer diameter (O.D.) ranges from ~100 nm to ~800 nm while maintaining uniform nanoscale channel apertures across all four barrels.

These images confirm the reproducibility and controllability of the fabrication process, enabling precise adjustment of multichannel electrode geometry with well-preserved nanoscale features and uniform channel separation.

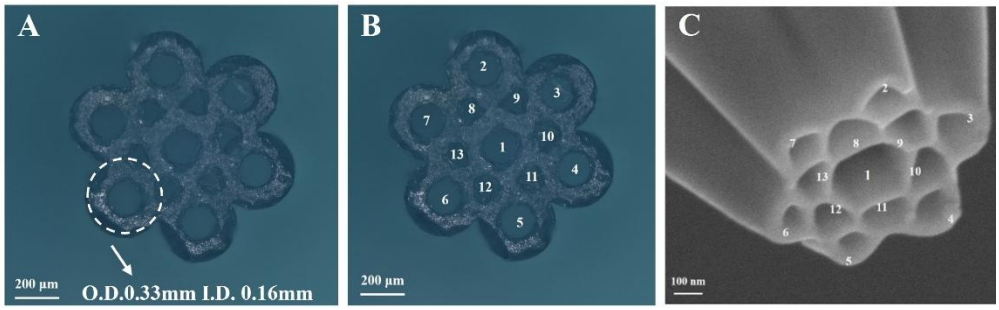

Figure S2. (A, B) Optical microscopy images of the end-face of the 7-barrel quartz capillary (Sutter Instrument, 7Q033-16-10; per barrel O.D. 0.33 mm, I.D. 0.16 mm; overall outer diameter ~1 mm). (C) SEM image of carbon-deposited 13-channel nanoelectrode tip.

Modeling of the electrochemical response of the multichannel carbon nanopipettes

Before presenting the results of the numerical simulations, it is important to consider a theoretical point related to the electrochemical response of pipette-based systems. For simplicity of the arguments, it will be considered for the case of straight cylindrical pipette with a single orifice (Figure S3), but the outcomes will be relevant to straight or conical θ- and ⊗-pipettes.

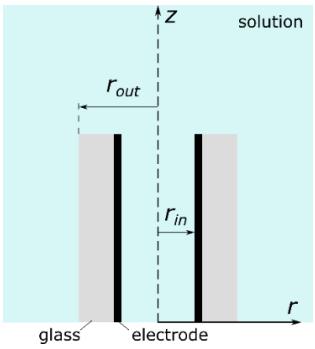

Figure S3. Schematics of a straight cylindrical pipette.

The response of the system consists of two contributions[5,6]:

(i) thin-layer like contribution due to the oxidation/reduction of the redox probe within the finite internal volume of the pipette giving rise to a bell-shape response;

(ii) disk-like contribution due to the transport of the redox probe from bulk solution through the pipette orifice towards pipette interior resulting in sigmoid steady-state response.

As the experimental data suggest that slow electron transfer is involved (see Fig.S7 below), the following analysis will be limited for the case of irreversible electron transfer (ET), while similar evaluations can be made for the case of quasireversible ET.

For the thin-layer-like contribution the peak potential, E_p, and peak current, i_p, for irreversible ET are (these equations are exact since they are derived under assumptions that the scan rate is sufficiently slow to keep concentration constant across thin-layer cell, so they are geometry independent) [Bard & Faulkner]:

$$(1-\alpha)f\left(E_p - E_0\right) = \ln\left((1-\alpha)f\frac{V}{A}\frac{v}{k_0}\right) \quad (1a)$$

$$i_p = \frac{\alpha f}{2.718}Vvc_{bulk} \quad (1b)$$

where α is the transfer coefficient, $f = F/RT$, E_0 is the formal potential of the redox couple, V is the volume of the thin-layer system, A is the surface area of the electrode, v is the scan rate, k_0 is the standard rate constant of ET and c_{bulk} is the redox probe bulk concentration.

At the same time the half-wave potential, $E_{1/2}$, of the steady-state current at disk electrodes (modeling here the transport through the pipette orifice towards the pipette interior) for an irreversible ET is[7]:

$$exp(\alpha\theta_h)\left[1 - exp(-\theta_h)\right] = 1.38\frac{D}{k_0\, r_0} \quad (2a)$$

$$i_{st.st} = 4FDc_{bulk}r_0 \quad (2b)$$

where $\theta_h = f(E_{1/2} - E_0)$, D is the redox probe diffusion coefficient (assumed to be equal for oxidized and reduced forms), r_0 is the disk radius (i.e. pipette orifice in the considered case).

The equation (2a) is a non-linear one, yet for $(E_{1/2} - E_0) \geq 100$ mV it can be approximated as

$$exp(\alpha\theta_h) = 1.38\frac{D}{k_0\, r_0} \quad => \quad \alpha\theta_h = \alpha f(E_{1/2} - E_0) = ln\left(1.38\frac{D}{k_0\, r_0}\right) \quad (3)$$

The equation (1) and (3) thus govern relative positions of the two contributions in the overall response of the pipette. For the practical purpose let us introduce a dimensionless parameter:

$$\gamma = log_{10}\left(1.38\frac{D}{r_0}\frac{A}{\alpha f V v}\right) (4)$$

For a straight cylindrical pipette (Fig. S3) $A = 2\pi r_0 L$ and $V = \pi r_0^2 L$, hence parameter γ is related to usually used dimensionless scan rate σ

$$\gamma = log_{10}\left(2.76\frac{D}{r_0^2}\frac{1}{\alpha f v}\right) = \log_{10}\left(\frac{2.76}{\alpha}\sigma\right), \text{ where } \sigma = \frac{D}{r_0^2}\frac{1}{fv} \quad (5)$$

Thus, the greater (smaller) γ is than zero, the more positive (negative) $E_{1/2}$ will be than E_p. This is illustrated in Fig.S4 for different values of γ, whose value was varied solely by changing the scan rate. The peak potential values are 0.04 V (Fig. S4a), 0.125 V (Fig. S4b) and 0.24 V (Fig. S4c). Note the variation of the relative values of the peak and steady state currents, since in accordance with Eqs. (1b) and (2b) peak current is proportional to v while steady state current is independent of the scan rate.

Note that the red curve is evaluated as the flux through the pipette orifice at a given time point, while converted to the current for comparison with the total current. This approximates the disk-like contribution as it assumes that molecules passed through the orifice almost instantly undergo ET (in general, for each flux line the times between passage of the orifice and actual ET events at the pipette internal wall will depend on radial position). The thin-layer component is obtained by subtracting the red curve (disk-like contribution) from the black curve (total current), and is therefore also approximate.

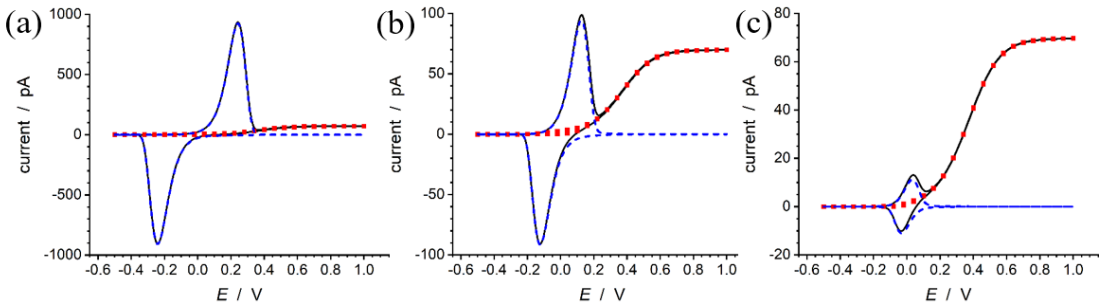

Figure S4. Cyclic voltammograms for cylindrical pipette with (a) $\gamma = 1.3$ ($v = 100$ V/s), (b) $\gamma = 2.3$ ($v = 10$ V/s), (c) $\gamma = 3.3$ ($v = 1$ V/s). Black curve – total current, red symbols – current through pipette orifice, blue dash – thin-layer-like contribution (it is defined as difference between black and red curves). Other parameters: $r_{in} = 225$ nm, $r_{out} = 250$ nm, $h_{ppt} = 60$ μm, $D = 7.6 \times 10^{-6}$ cm^2/s, $c_{bulk} = 1$ mM, $k_0 = 2 \times 10^{-4}$ cm/s.

The four-channel conical pipette electrochemical behavior will follow the same general principles although exact coefficient might differ. Simulation of ⊗-pipette response for the case of n-electron transfer reaction

$$A \underset{k_b}{\overset{k_f}{\rightleftarrows}} B + ne^- \quad (6)$$

taking place at all pipette internal boundaries were performed in COMSOL, where we set up a 3D model as shown in Fig. S5 (note the problem is intrinsically 3D for any number of channels active).

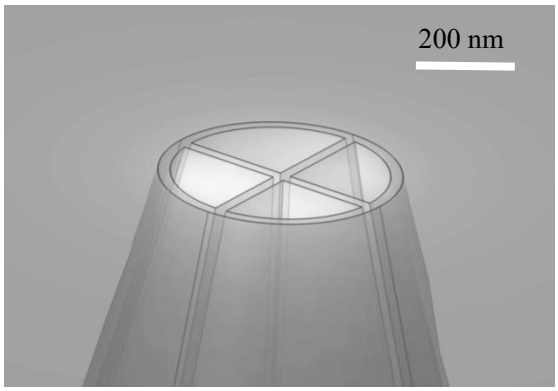

Figure S5. COMSOL 3D model of a four-channel open CNP with outer diameter of 500 nm and inner diameter of 450 nm.

For this end, the diffusion equation was solved

$$\frac{\partial c}{\partial t} = D\left[\frac{\partial^2 c}{\partial x^2} + \frac{\partial^2 c}{\partial y^2} + \frac{\partial^2 c}{\partial z^2}\right] (7)$$

with the following initial and boundary conditions:

$t = 0$: $\forall x, y, z$ in solution $c = c_{bulk}$ (8a)

$t > 0$: $\forall x, y, z$ at carbon $D\frac{\partial c}{\partial \vec{n}} = k_f c - k_b(c_{bulk} - c)$ (8b)

$\forall x, y, z$ at insulator $D\frac{\partial c}{\partial \vec{n}} = 0$ (8c)

$x^2 + y^2 + z^2 \to \infty \; c \to \infty$ (8c)

where k_f and k_b are Butler-Volmer forward and backward ET rate constants:

$$k_f(t) = k_0 \exp[(1-\alpha)nf(E(t) - E_0)] \quad k_b(t) = k_0 \exp[-\alpha nf(E(t) - E_0)] \quad (9)$$

where potential varies linearly between E_1 and E_2 potentials for m cycles:

$$E(t) = E_2 - v\left|\left(t - \left\lfloor\frac{t}{t_{cycle}}\right\rfloor * t_{cycle}\right) - \frac{t_{cycle}}{2}\right| \quad (10)$$

where $t_{cycle} = 2(E_2 - E_1)/v$ is the time duration of one cycle and $\lfloor \quad \rfloor$ is the 'floor' function, i.e. rounding operation to the lowest integer.

Reversible redox probe – FcMeOH

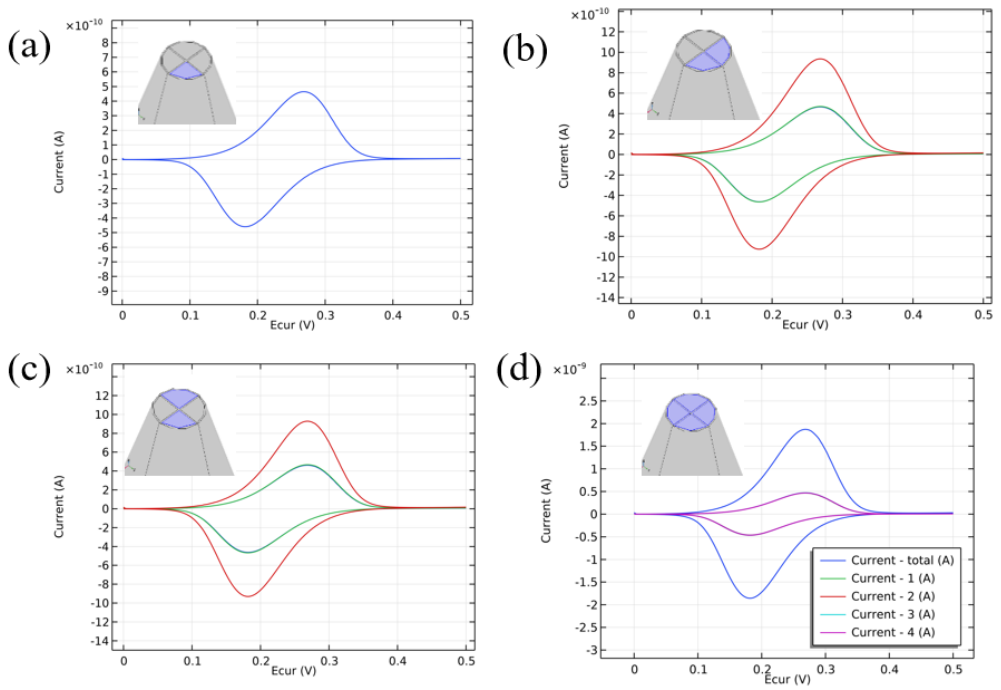

Figure S6. Voltammorgrams for the cases when (a) only one channel, (b) two neighbouring, (c) two opposite or (d) all four channels are biased. Note that currents corresponding to individual channels are superimposed. See simulation parameters in the text.

Fig. S6 shows simulated currents for FcMeOH, a reversible redox probe, when one or several pipette channels were biased. Note that each sub-figure in Fig.S6 shows 4 consecutive CV cycles, however, since progressive increase of solution volume in the pipette with the repetitive scans (as observed in the experiment, see Fig. S7) is not taken into account, the CVs superimpose for all cycles. [6]

The simulated parameters were as follows: $r_{in} = 225$ nm, $r_{out} = 250$ nm, $\beta = 15°$ (pipette angle), $h_{ppt} = 85$ µm, $D = 7.6 \times 10^{-6}$ cm^2/s[8], $c_{bulk} = 1$ mM, $k_0 = 2 \times 10^{-4}$ cm/s, $n = 1$, $\alpha = 0.5$, $E_0 = 0.225$ V, $v = 50$ mV/s, $m = 4$ (number of CV cycles).

The fits at Fig.S6 qualitatively fit the data in Fig.S7. At the same time parameter $\gamma > 3$ (evaluated via Eq.(4)) for parameters just given above, which means that $E_{1/2}$ is significantly more positive than E_p (see Fig. S4).

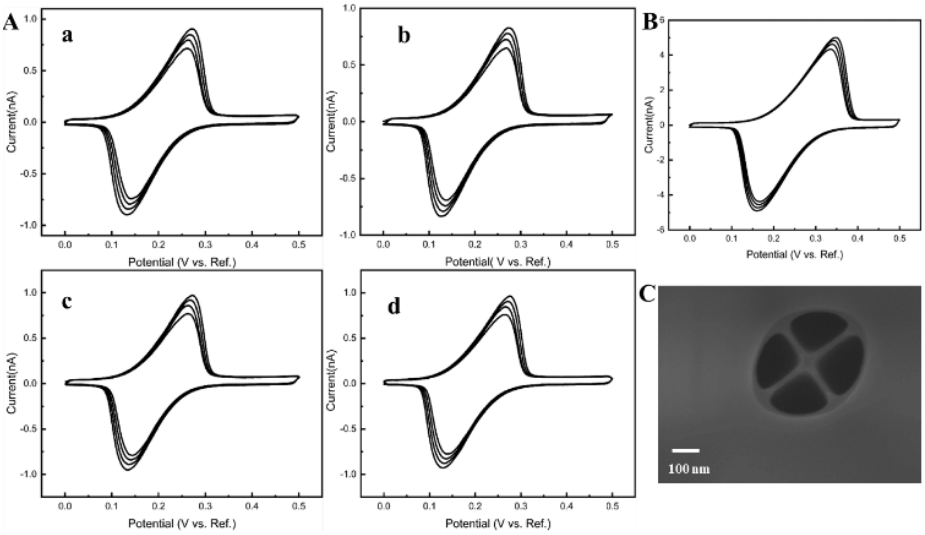

Figure S7. (A) Individual cyclic voltammograms (CVs) recorded from each of the four channels of a single open CNPs in 1 mM FcMeOH with 100 mM KCl (Reference electrode, Ag/AgCl). (B) CVs recorded from the same open CNP with all four channels connected simultaneously to a single working-electrode input. (Inset) SEM image of the tip showing four hollow carbon channels with nanoscale spacing.

Reversible probe – 4 disk electrodes (filled type)

Here we model the response of the filled-type carbon nanopipette four channels electrode (see Fig. 3 in the main text). The simulated parameters were as follows: $r_{out} = 350$ nm, $\beta = 15°$ (pipette angle), $h_{ppt} = 60$ µm, $r_{disk} = 85$ nm, $x_{disk} = y_{disk} = 140$ nm (each disk center offset with respect to the center of the tip), $D = 7.6 \times 10^{-6}$ cm^2/s, $c_{bulk} = 1$ mM, $k_0 = 2 \times 10^{-4}$ cm/s, $n = 1$, $\alpha = 0.5$, $E_0 = 0.225$ V, $v = 50$ mV/s, $m = 2$ (number of CV cycles). Simulated currents for individual disks and all four electrodes are shown in Fig.S8. Fig.S9 displays the concentration distribution in the cross-section passing through the symmetry axis of the pipette and centers of two electrodes. Top view of disks locations at the pipette tip are shown in the inset of Fig. S8.

Note that Fig. S10 compares responses of single electrodes for the configurations when only one channel is active and all four channels are active. As can be seen the steady-state current at single active channel is significantly larger due to the absence of competing neighboring electrodes.

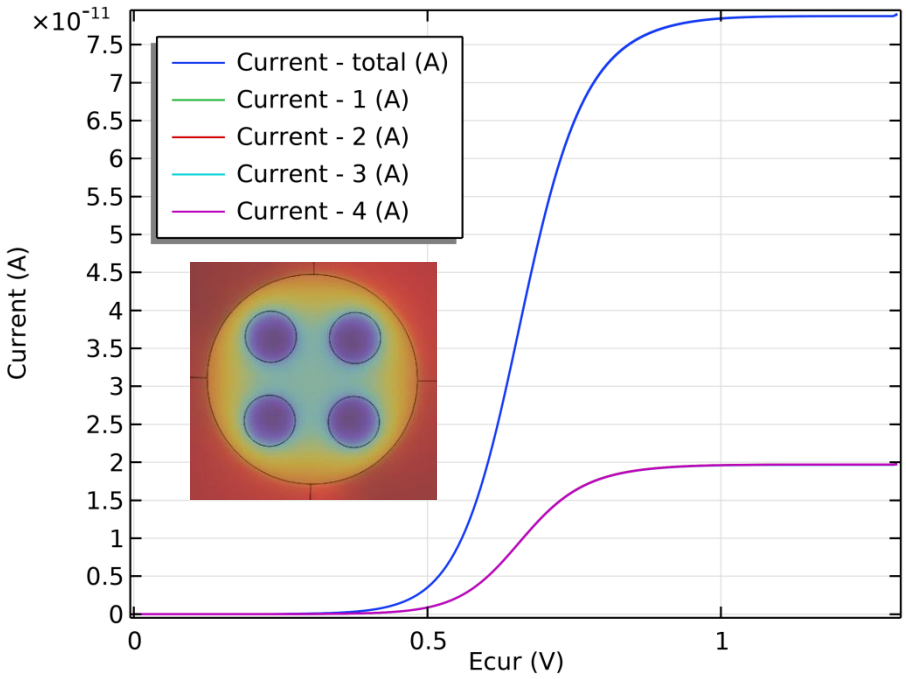

Figure S8. Voltammorgrams for the case when all four electrodes are biased. Note that currents corresponding to individual electrodes are superimposed. See simulation parameters in the text.

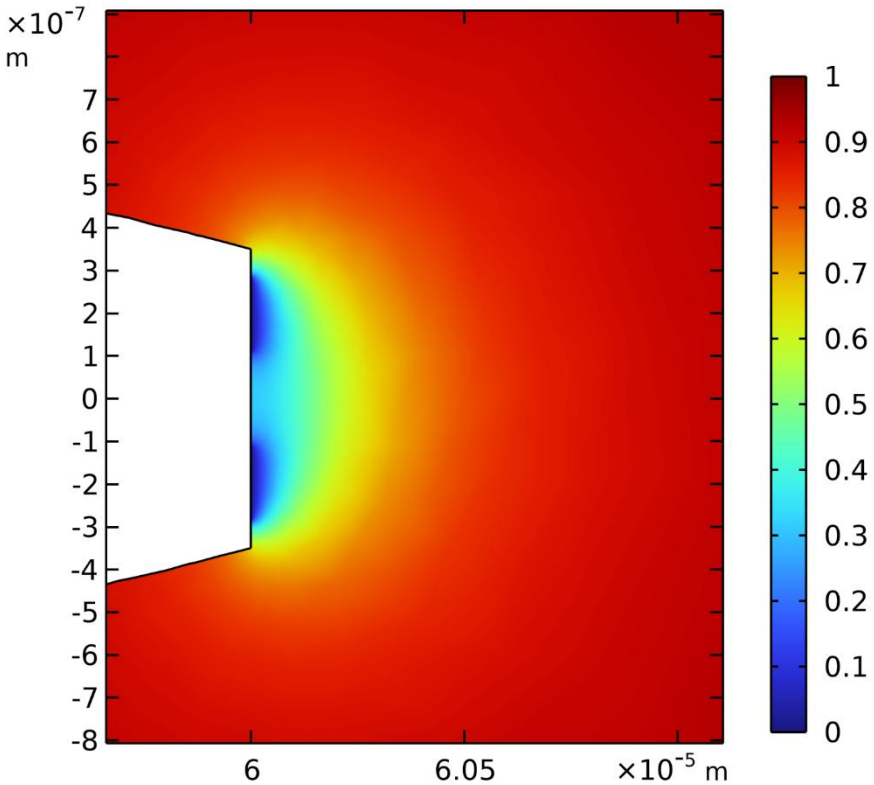

Figure S9. Concentration distribution for the case when all four electrodes are biased. The cross-section plane is passing through the tip symmetry axis and centers of two electrodes. Same parameters as for Fig.S8, $E = 1.3$ V ($t = 26$ s), i.e. at potential switching point.

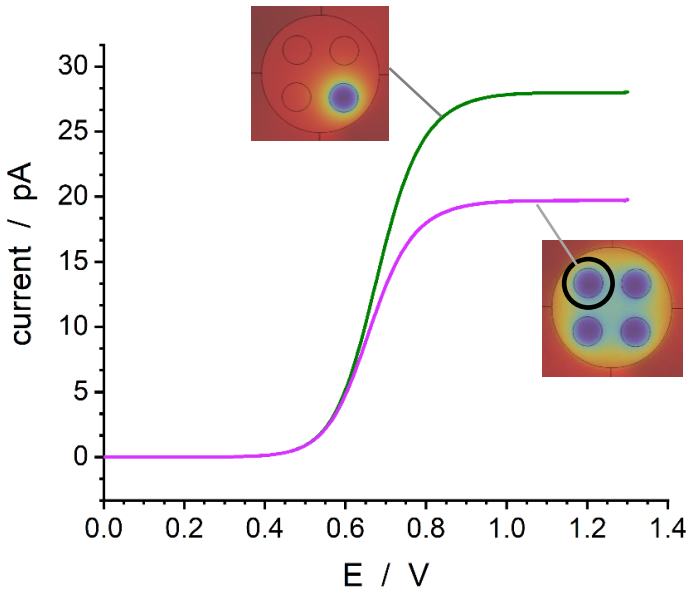

Figure S10. Comparison of the currents at a single disk for the cases when only 1 disk (green) or all 4 disks (magenta) are active. It illustrates how interference between the neighboring disks decrease the current of the individual electrodes (magenta) comparing to the case when interference is absent (green).

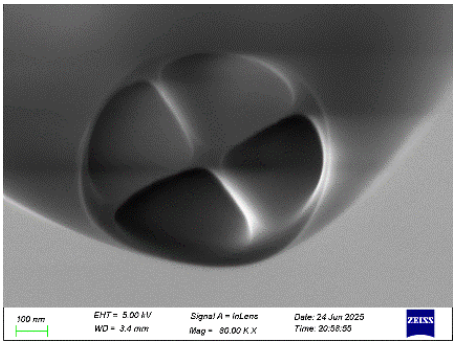

Figure S11. Representative SEM image of a four-channel open carbon nanopipette (CNP) used for VIEC measurements (overall diameter, ~800 nm; single-orifice diameter, ~320 nm.)

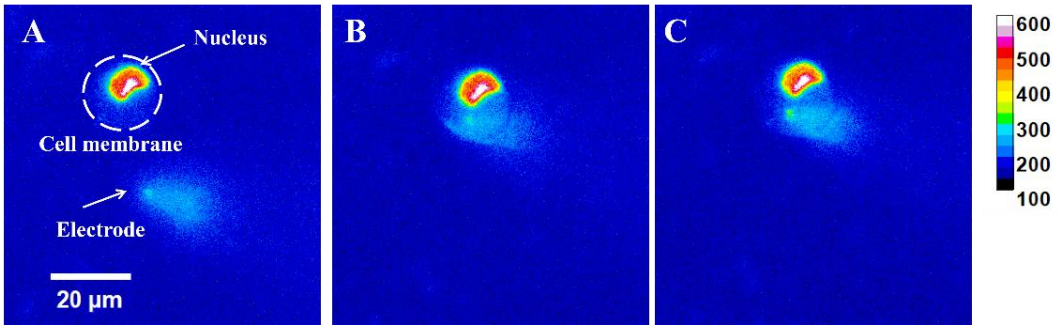

Figure S12. Fluorescence heat maps illustrating the positioning of the nanoelectrode relative to a single cell, confirming the insertion depths for parallel intracellular measurements near the plasma membrane and the nucleus. (A) The nucleus was stained with Hoechst 33342, and the electrode tip was labeled with tetraphenylethylene, showing the electrode positioned at a distance from the cell.

(B) The electrode was advanced to make gentle contact with the plasma membrane, as indicated by a slight displacement of the cell upon contact. (C) The electrode was further inserted into the cytoplasm and positioned between the plasma membrane and the nucleus, verifying the appropriate depth for intracellular measurements.

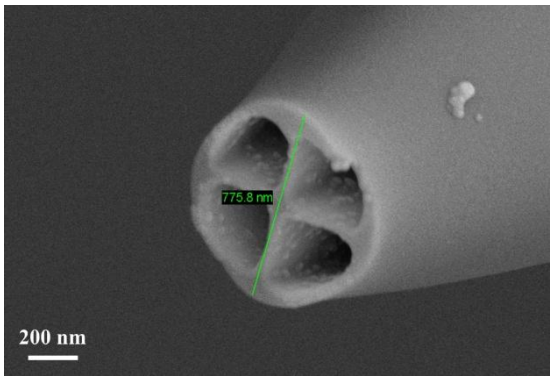

Figure S13. Representative SEM image of four-channel hollow carbon nanopipette used for intracellular measurements showing an overall outer diameter of ~780 nm. The diameter of each individual channel is approximately 300 nm, and the wall thickness between adjacent channels is ~60 nm.

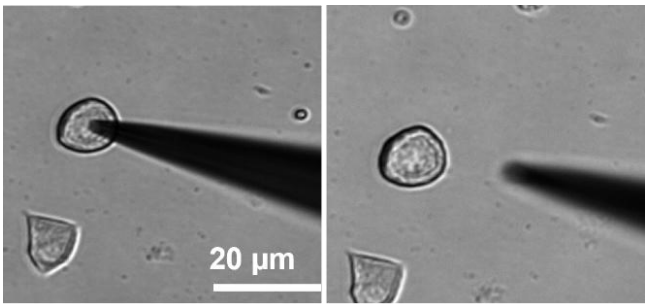

Figure S14. Representative bright-field microscopic images taken during electrode insertion and after open CNP removal, showing that the cell membrane keeps its integrity (see also Fig.S15 for trypan blue test).

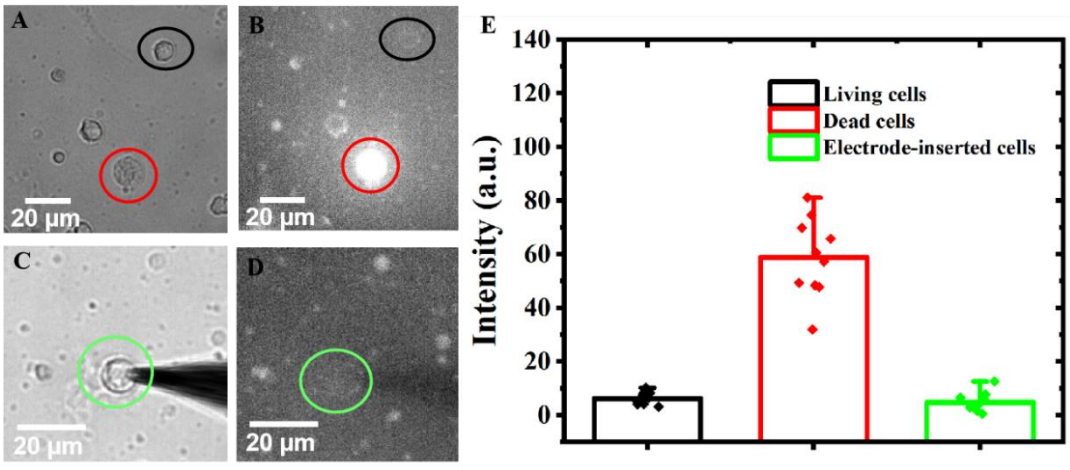

Figure S15. Validation of nondestructive four channel open CNPs insertion in live cells using trypan

blue exclusion. (A, B) Bright-field (A) and corresponding fluorescence (B) images (λ_ex = 480 nm, λ_em = 575 nm) of a mixed population of live (circled in black) and dead (circled in red) cells. Dead cells with compromised membranes were stained and exhibited strong fluorescence, whereas live cells excluded the dye and remained nonfluorescent. (C, D) Bright-field (C) and fluorescence (D) images of a live cell after nanoelectrode insertion. The absence of fluorescence in (D) indicates that the cell membrane integrity was preserved after electrode penetration. (E) Quantitative fluorescence intensity analysis of live cells (n = 10), dead cells (n = 10), and electrode-inserted live cells (n = 10), confirming the nondestructive nature of electrode insertion (error bars represent standard deviation).

Based on the observations in Figures S14 and S15, the multichannel hollow nanoelectrode exhibits similar noninvasive and minimally perturbative characteristics as the single-channel hollow configuration. The ultrathin insulating sheath and smooth tapered geometry reduce insertion-induced mechanical stress, enabling gentle penetration without compromising the plasma membrane. Moreover, the hollow structure allows shallow insertion—only to the region between the plasma membrane and the nuclear envelope—while still achieving efficient intracellular access. Once positioned in this perinuclear region, cytoplasmic vesicles can diffuse or be drawn by capillary forces into the hollow channel, where they interact with the extensive electroactive inner surface for high-efficiency electrochemical detection.

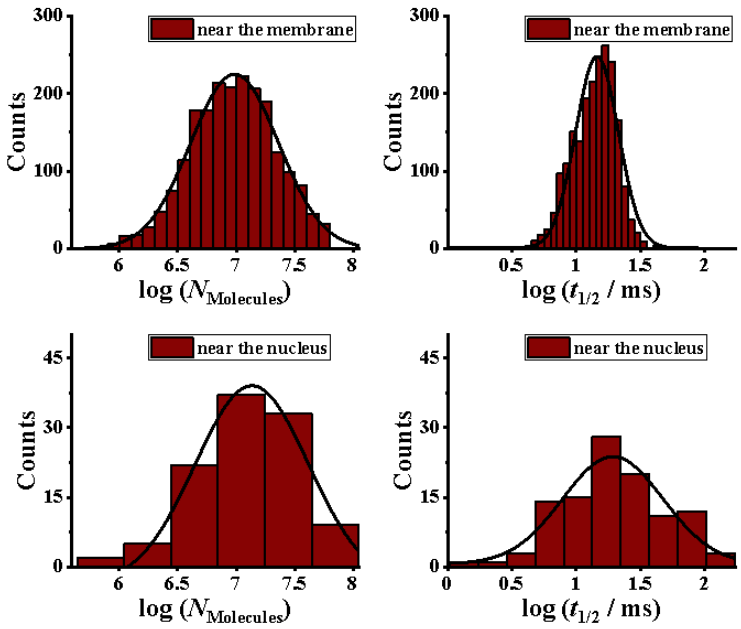

Figure S16. Distributions of vesicular release parameters from intracellular measurements at two subcellular regions. (A, B) Distributions of log ($N_{molecules}$) and log ($t_{1/2}$) recorded from the membrane-proximal region. (C, D) Corresponding distributions of log ($N_{molecules}$) and log ($t_{1/2}$) recorded from the perinuclear region. Each histogram was fitted with a Gaussian function on the log scale (solid line). Compared with the membrane-proximal region, spikes recorded near the nucleus exhibited larger $N_{molecules}$ and longer $t_{1/2}$, indicating a higher vesicular content but slower release kinetics.

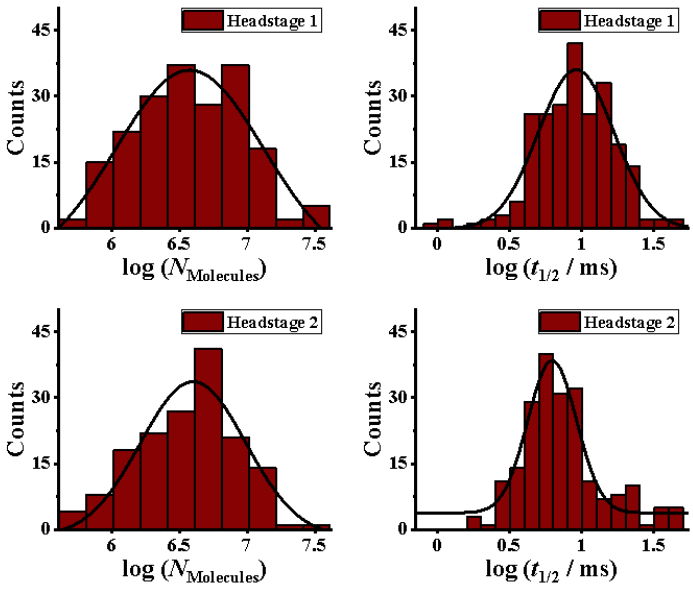

Figure S17. Statistical distributions of vesicular release parameters obtained from intracellular measurements under the control configuration. (A, B) Distributions of log ($N_{molecules}$) and log ($t_{1/2}$) recorded from the left-side region of the cell. (C, D) Corresponding distributions of log ($N_{molecules}$) and log ($t_{1/2}$) recorded from the right-side region of the same cell. Each histogram was fitted with a Gaussian function on the log scale (solid line). No significant difference was observed between the two regions.

References

1. O'Connor, D. T., Mahata, S. K., Mahata, M., Jiang, Q., Hook, V. Y., and Taupenot, L. Nat. Protoc. 2007, 5, 1248−1253.

2. Pardo, M. R., Estévez-Herrera, J., Castañeyra, L., Borges, R., and Machado, J. D. Anal. Biochem. 2017, 536, 1−7.

3. Dunevall, J.; Fathali, H.; Najafinobar, N.; Lovric, J.; Wigström, J.; Cans, A.-S.; Ewing, A. G. J. Am. Chem. Soc. 2015, 13, 4344- 4346.

4. Mosharov, E., and Sulzer, D. Nat. Methods 2005, 9, 651−658.

5. Yu, Y.; Noël, J.M.; Mirkin, M.V.; Gao, Y.; Mashtalir, O.; Friedman, G.; Gogotsi, Y. *Anal. Chem.* 2014, 86, 3365–3372.

6. Laucirica, G.; Crespo, G. A.; Cuartero, M. *Anal. Chem.* 2025, 97, 17659–17667.

7. Aoki, K. Electrochem. Commun. 2005, 7, 523–527

8. Ma, W.; Hu, K.; Chen, Q.; Zhou, M.; Mirkin, M.V.; Bard, A.J. Nano Lett. 2017, 17, 4354–4358.